



How turbulence increases the bubble–particle collision rate

Linfeng Jiang¹  and Dominik Krug¹ 

¹Physics of Fluids Group, Max Planck Center Twente for Complex Fluid Dynamics and Johannes Martinus Burgers Centre for Fluid Dynamics, University of Twente, 7500 AE Enschede, the Netherlands

Corresponding author: Dominik Krug, d.j.krug@utwente.nl

(Received 27 August 2024; revised 29 October 2024; accepted 27 December 2024)

We study the effect of turbulence on collisions between a finite-size bubble and small inertial particles based on interface-resolved simulations. Our results show that the interaction with the flow field around the bubble remains the dominant effect. Nonlinear dependencies in this process can enhance the turbulent collision rate by up to 100 % compared to quiescent flow. Fluctuations in the bubble slip velocity during the interaction with the particle additionally increase the collision rate. We present a frozen-turbulence model that captures the relevant effects providing a physically consistent framework to model collisions of small inertial particles with finite-sized objects in turbulence.

Key words: isotropic turbulence

1. Introduction

Bubble–particle collisions are central to the flotation process, which is widely used (e.g. in the mining industry) to separate minerals through their attachment to rising bubbles. This intricate process involves a wide range of colloid science disciplines (Derjaguin & Dukhin 1993; Nguyen & Schulze 2003; Kostoglou, Karapantsios & Oikonomidou 2020*b*), with significant complexity stemming from the interplay of hydrodynamics and physicochemical interactions. The hydrodynamic bubble–particle interaction remains of paramount importance for optimisation, as it is the rate-determining step that also sets the conditions for other interactions.

Most of the work on bubble–particle collisions draws on the large body of work on particle–particle collisions (Pumir & Wilkinson 2016), in particular the seminal work of Saffman & Turner (1956) for the tracer limit and the model proposed by

Abrahamson (1975) for the kinetic gas limit at large particle inertia. Such models predict the collision rate without considering the hydrodynamic interaction between the collision partners, but must take into account effects such as the segregation of bubbles and particles in a turbulent flow (Chan, Ng & Krug 2023). However, the significant size difference between the larger bubble and the mineral particles in a typical flotation process makes it important to account for the flow distortion around the bubble. This can cause an encountering particle to be deflected, reducing the actual number of collisions. For a bubble rising in quiescent flow, this process is deterministic and has been studied widely (Schulze 1989; Nguyen & Schulze 2003; Sarrot, Guiraud & Legendre 2005; Huang, Legendre & Guiraud 2012). In this case, the effect of the hydrodynamic interaction can be captured in terms of a collision efficiency, which relates the rate of actual collisions to the encounter rate. The lack of a suitable concept to account for turbulence in this context is widely acknowledged in the literature (Pyke, Fornasiero & Ralston 2003; Nguyen *et al.* 2016; Hajisharifi, Marchioli & Soldati 2021). Existing approaches are flawed because they combine turbulent encounter rates with collision efficiencies applicable to pure gravitational settling (Bloom & Heindel 2002; Koh & Schwarz 2007; Liu & Schwarz 2009; Yoon *et al.* 2016). Others use a Reynolds-type decomposition, which is problematic given the strongly nonlinear dependence of the problem on the flow velocity. Another conceptual inconsistency is that the encounter rate is based on the bubble–particle relative velocity, whereas the collision efficiency is determined by the bubble slip relative to the fluid. Some of these deficiencies are overcome by the collision model presented in Kostoglou, Karapantsios & Evgenidis (2020a), but this, however, remains limited to tracer particles.

The core problem is to determine the collision rate of small inertial particles with a finite-size object in a turbulent flow. This is of general relevance to many other applications beyond flotation, such as the collision of cloud droplets (Falkovich, Fouxon & Stepanov 2002; Poydenot & Andreotti 2024), the accretion of planetesimals by the collection of dust particles (Guillot, Ida & Ormel 2014; Homann *et al.* 2016), depth filtration (May & Clifford 1967; Cushing & Lawler 1998), or bacterial degradation of marine snow (Arguedas-Leiva *et al.* 2022). However, the scarcity of data, due to the difficulties in performing the necessary experiments and interface-resolved simulations, has hindered the progress of theoretical research in this area. In this paper, we present a combined numerical and theoretical study of the effects of turbulence on bubble–particle collisions using direct numerical simulations. We adopt homogeneous and isotropic turbulence (HIT), in which we measure how turbulent fluctuation modifies the bubble–particle collision rate along the bubble–rising path.

2. Statistical model

The collision frequency K of particles with a bubble is determined by $K = \Gamma n_p$, where n_p is the particle number density, and the proportionality coefficient Γ ($\text{m}^3 \text{s}^{-1}$) is commonly referred to as the collision kernel and is determined by the flow (Pumir & Wilkinson 2016). In quiescent flow, the collisions between a spherical bubble of radius r_b rising at constant velocity U_b with small inertial solid particles are deterministic. The particle grazing trajectory ψ_c determines a ‘collision tube’, where all the particles contained inside collide with the bubble, as illustrated in figure 1(a). In this case, the collision frequency is determined by the collision number flux, i.e. $K = Q_c n_p$. The collision number flux Q_c can be determined by the cross-sectional area of radius r_c limited by the grazing trajectories upstream far from the bubble: $Q_c = \pi r_c^2 U_b$. Therefore, the collision kernel in quiescent flow can be expressed as $\Gamma_q = Q_c = \pi r_b^2 U_b E_c$, where the collision efficiency $E_c = r_c^2 / r_b^2$ measures the ratio of collided particle number to the total encountering particle number.

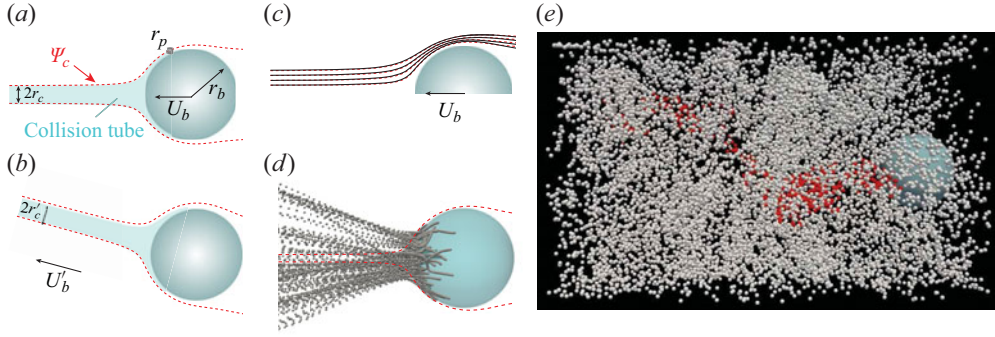


Figure 1. (a) Sketch of the grazing trajectory (red dashed line) in quiescent flow. The shaded region indicates the collision tube where all particles collide on the bubble. (b) Sketch of the bubble–particle collision model under temporary bubble slip velocity U'_b . (c) Mean flow streamlines around the bubble for the case of imposed velocity bubble (solid) and quiescent flow (dashed lines) at $Re_b = 120$. (d) Trajectories of colliding particles ($r_p/r_b = 0.05$, $St_p = 0.04$) for the case of imposed velocity bubble compared to the corresponding grazing trajectories (red lines) in quiescent flow at the same $Re_b = 120$. (e) Snapshot of the bubble–particle collision process in turbulence for the imposed-velocity bubble with flow from left to right in the bubble frame of reference. Incoming particles that end up colliding with the bubble are marked in red.

Notice here that E_c depends on the bubble Reynolds number $Re_b = 2r_b U_b / \nu$, the ratio of the particle radius r_p and r_b , and the Stokes number $St_p = \tau_p / \tau_f$, with τ_p the particle response time, and $\tau_f = 2r_b / U_b$ the time scale of the bubble–particle interaction (Dai, Fornasiero & Ralston 2000; Sarrot *et al.* 2005; Huang *et al.* 2012).

To provide an understanding of the relevant physical mechanisms of bubble–particle collision in turbulence, we propose a statistical model. We start from the assumption that the flow field in the vicinity of the bubble is approximately stationary and uniform during the bubble–particle interaction. Conceptually, this implies that the temporal scale τ_f is (much) shorter than the correlation time scale of flow fluctuations ($O(\tau_\eta)$), but it remains to be tested from the data under what conditions exactly this assumption is valid in practice. Additionally, we consider the flow correlation length scale to be comparable to or larger than the bubble size. Within this ‘frozen turbulence’ assumption, the instantaneous bubble–particle collision process in turbulence can be related back to that observed in quiescent flow. Therefore, the equivalent steady flow problem is characterised by the magnitude of the instantaneous bubble slip velocity U'_b with corresponding values $Re'_b = 2r_b U'_b / \nu$ and $St'_p = \tau_p / (2r_b / U'_b)$, as shown in figure 1(b). The entire bubble–particle collision process in a turbulent flow can then be viewed as a superposition of collision events in quiescent flow with varying parameters Re'_b and St'_p . In the framework, the collision number $N_c|_{\Delta\tau}$ during a short period $\Delta\tau$ ($O(\tau_\eta)$) in turbulent flow, with mean particle number density n_p , is given by $N_c|_{\Delta\tau} = \pi r_b^2 E_c(Re'_b, St'_p) U'_b n'_p \Delta\tau$, where n'_p is the instantaneous encountering particle number density, which depends on Re'_b and St'_p . Importantly, $E_c(Re'_b, St'_p)$ denotes the collision efficiency in quiescent flow for varying flow parameters, which is deterministic and can be parametrised. Then the total expected collision number N_c during a sufficiently long time period $T = \sum \Delta\tau$ is given by

$$N_c = \pi r_b^2 T \int E_c(Re'_b, St'_p) U'_b f(U'_b) n'_p dU'_b. \quad (2.1)$$

Simulation cases	Re_λ	$\eta/\Delta x$	$\tau_\eta/\Delta t$	L/η	T_L/τ_η	λ/η	$\overline{Re_b}$	T_i
Imposed-velocity bubble	32	8	780	27.3	9.1	11.6	120	0.25
Freely rising bubble	32	8	780	27.3	9.1	11.6	110	0.27
Freely rising bubble	64	4	780	67.9	16.7	16.2	150	0.53

Table 1. Parameter of the numerical simulations and relevant turbulence scales: Re_λ is the Taylor–Reynolds number; $\eta = (v^3/\epsilon)^{1/4}$ is the Kolmogorov dissipation length scale in grid space units Δx ; τ_η is the Kolmogorov time scale in time-step units Δt ; $L = u'^3/\epsilon$ is the integral scale; $T_L = L/u'$ is the large-eddy turnover time; $\lambda = u'\sqrt{15\nu/\epsilon}$ is the Taylor micro-scale; $\overline{Re_b} = 2r_b\overline{U_b}/\nu$ is the bubble Reynolds number based on the mean rising velocity $\overline{U_b}$; $T_i = u'/\overline{U_b}$ is the turbulent intensity.

Based on this, the collision kernel can be derived as

$$\Gamma = \frac{K}{n_p} = \frac{\pi r_b^2}{n_p} \int E_c(Re'_b, St'_p) U'_b f(U'_b) n'_p dU'_b. \quad (2.2)$$

Note that collision efficiency has been studied extensively, and the general dependence of E_c on the bubble Reynolds number and particle Stokes number has been established in the literature (Schulze 1989; Sarrot, Guiraud & Legendre 2005; Huang *et al.* 2012). The collision kernel is thus determined by the probability density function (PDF) $f(U'_b)$ of the bubble slip velocity U'_b , the modelling of which remains an open question. Furthermore, we note that the collision kernel will also be affected by the preferential sampling for particles with large St_p , as this alters the incoming particle number density.

3. Numerical methods and simulations

We perform interface-resolved direct numerical simulations (DNS) to test this model. The turbulent flow is governed by the incompressible Navier–Stokes equations, which read

$$\frac{\partial \mathbf{u}}{\partial t} + \mathbf{u} \cdot \nabla \mathbf{u} = -\frac{1}{\rho_f} \nabla p + \nu \nabla^2 \mathbf{u} + \mathbf{f} + \mathbf{f}_b, \quad (3.1)$$

$$\nabla \cdot \mathbf{u} = 0, \quad (3.2)$$

where \mathbf{u} is the fluid velocity, p denotes the pressure, and the parameters are the kinematic viscosity ν and the reference liquid density ρ_f . The vector \mathbf{f} denotes an external random large-scale volume force, which is statistically homogeneous and isotropic, with constant-in-time global energy input (Perlekar *et al.* 2012). This force is used to generate and maintain the turbulent flow. The bubble-free turbulent flow intensity is characterised by the Reynolds number based on the Taylor microscale, $Re_\lambda = \sqrt{15u'}/(\nu\epsilon)$, where u' denotes the root mean square velocity of the turbulence, and ϵ is the mean energy dissipation rate. The vector \mathbf{f}_b accounts for the bubble–fluid two-way coupling.

In the practice of flotation, commonly a large amount of surfactants is present in the liquid. Therefore, it is reasonable to assume that the bubbles with a typical Reynolds number below 200 are fully contaminated and approximately spherical, resulting in a boundary condition that is nearly no-slip (Nguyen & Schulze 2003; Huang *et al.* 2012). The Weber number $We = 2r_b\rho_f U_b^2/\chi$ based on the surface tension χ of water and the bubble rise velocity is $O(0.1)$ for our simulations, and even lower based on turbulent fluctuations. Therefore, bubble deformations remain negligible even if surface tension is lowered by the presence of surfactants. Under these conditions, the bubble behaves

similarly to buoyant spheres. In this case, the translation and rotation of the bubble are governed by the Newton–Euler equations

$$m_b \frac{d\mathbf{U}_b}{dt} = \oint_{S_b} \boldsymbol{\sigma} \cdot \mathbf{n} dS + V_b(\rho_b - \rho_f)\mathbf{g}, \quad (3.3)$$

$$\frac{d\mathbf{I}\boldsymbol{\Omega}}{dt} = \oint_{S_b} (\mathbf{x} - \mathbf{x}_b) \times (\boldsymbol{\sigma} \cdot \mathbf{n}) dS, \quad (3.4)$$

where $\mathbf{U}_b(t) = d\mathbf{x}_b/dt$ and $\boldsymbol{\Omega}(t)$, respectively, are the bubble velocity and angular velocity vectors at position $\mathbf{x}_b(t)$. The bubble mass is given by $m_b = \rho_b V_b$ (where ρ_b is the bubble density, and V_b is the volume), and \mathbf{I} is the moment of inertia tensor. Here, $\boldsymbol{\sigma} = -p\mathbf{I} + \rho\nu(\nabla\mathbf{u} + \nabla\mathbf{u}^T)$ is the fluid stress tensor, $\mathbf{x} - \mathbf{x}_b$ is the position vector relative to the bubble centre, and \mathbf{n} is the outward-pointing normal to the bubble surface S_b . This term $\boldsymbol{\sigma}$ is solved by the immersed boundary method (IBM) to account for the two-way coupling between the flow and the bubble. In the last decades, the IBM has been used widely for studying the multi-phase flow (Peskin 2002; Mittal & Iaccarino 2005; Uhlmann 2005). In the IBM, the Euler grids of the fluid are fixed, and the surface of the bubble is represented by Lagrangian nodes that move with the bubble motion. To avoid the formation of a mean flow due to the buoyancy driving exerted by the bubble, we compensate the average force applied from the bubble to the liquid to attain a statistically stationary state (Höfler & Schwarzer 2000; Chouippe & Uhlmann 2015). To achieve this, the spatial average of the IBM volume force term needs to be subtracted. More explicitly, we compute the average at each simulation time step:

$$\langle \mathbf{f}^{ibm} \rangle_{\Omega}(t) = \frac{1}{\|\Omega\|} \int_{\Omega} \mathbf{f}^{ibm}(\mathbf{x}, t) d\mathbf{x}, \quad (3.5)$$

where Ω denotes the entire computational domain, $\langle \cdot \rangle_{\Omega}$ indicates the spatial average over the entire Ω region, and $\|\Omega\|$ is the volume of the Ω region. Then the bubble-related contribution to the volume force, \mathbf{f}_b , is obtained from

$$\mathbf{f}_b(\mathbf{x}, t) = \mathbf{f}^{ibm}(\mathbf{x}, t) - \langle \mathbf{f}^{ibm} \rangle_{\Omega}(t). \quad (3.6)$$

We adopt an implicit method (Tschisgale, Kempe & Fröhlich 2017) to solve the bubble dynamics as the conventional explicit method is numerically unstable when the bubble is light (Uhlmann 2005). To avoid the build-up of momentum in the triply periodic domain over time, the force applied by the bubble on the liquid is compensated to attain a statistically stationary state (Chouippe & Uhlmann 2015).

We use a code based on the lattice Boltzmann method to solve the Navier–Stokes equations (Calzavarini 2019; Jiang *et al.* 2022). Two sets of simulations are carried out: (1) a simplified ideal configuration where a constant bubble velocity is imposed, and (2) simulations with a freely rising bubble, where the bubble–fluid density ratio is $\rho_b/\rho_f = 10^{-3}$. Matching practically relevant conditions (Wang *et al.* 2022), we consider a moderately turbulent flow ($Re_{\lambda} = 32$ and 64) and a bubble Reynolds number $Re_b \sim O(100)$. Detailed parameters of the simulations are summarised in table 1. There are two computational conditions that should be satisfied in the simulations. First, the wake of the fully contaminated bubble presents a steady axisymmetric vortex at such a high Re_b in a quiescent flow (Johnson & Patel 1999; Sarrot *et al.* 2005). As the flow domain is periodic, the incoming flow ahead of the bubble might be disturbed by the remnants of this bubble wake. To avoid this issue, the flow domain in the bubble rising direction should be sufficiently large. The whole flow domain adopted in this work is rectangular,

with uniform grid sizes $N_x \times N_y \times N_z = 3072 \times 512 \times 512$, where the bubble rises in the x -direction. We found that using this domain length was sufficient to avoid wake effect. Second, the number of lattices within the boundary layer of the bubble should be sufficient. The approximate boundary layer thickness is estimated as $\delta = 1.13/Re_b^{1/2}$ (Johnson & Patel 1999), where δ denotes the boundary layer thickness normalised by $2r_b$. Additionally, the minimum particle size ($r_p/r_b = 0.025$) should be larger than the lattice unit to ensure the accuracy of interpolation when the particle is close to the bubble. To this end, the bubble diameter is resolved by 80 grids to make sure that the boundary layer is well resolved, as well as the minimum distance of the point-like particle to the bubble being larger than one grid unit. The ratio of turbulent dissipation time scale τ_η to τ_f in our simulations is close to 1.2. We note that the typical auto-correlation time scale of the turbulent flow is longer than τ_η , which implies the validity of the assumption of frozen turbulence in our model. In the flotation process, the mineral particles are significantly smaller than the turbulent dissipation scale η . We represent these as one-way coupled point particles, considering the non-Stokesian drag force and the added mass force. We do not account for potential alterations to the drag force when a particle is close to the bubble surface. The particle response time $\tau_p = r_p^2/(3\beta\nu)$ includes the density coefficient $\beta = 3\rho_f/(\rho_f + 2\rho_p)$, where ρ_p denote the density of the particle. The particle dynamics is driven by the instantaneous turbulent flow. The collision frequency $K = N_c/T$, and thus the collision kernel $\Gamma = K/n_p$, is measured by counting the number of particles (N_c) that collide with the bubble over a long time period T . A collision is detected when the distance between the particle and bubble is smaller than $r_p + r_b$. Additionally, we conduct simulations of bubble–particle collisions in a quiescent flow at Re_b ranging from 80 to 210 to obtain the dependence of E_c on Re_b and St_p . In these simulations, a constant-velocity inflow is applied at the inlet, while a homogeneous Neumann boundary condition is imposed at the outlet. The bubble is fixed at the centre of the domain, and the spatial resolution is kept the same as for the turbulent flow case and the turbulence forcing term \mathbf{f} is switched off.

4. Results

We start from the discussion of the bubble with an imposed velocity. In figure 1(c), we demonstrate that the impact of turbulent fluctuations on the mean streamlines is insignificant for the present parameters. In particular, in the incoming flow, which determines the collision rate, the differences are very small, lending support to our modelling approach. More noticeable differences in the wake region are a consequence of turbulence disrupting the symmetric recirculation pattern behind the bubble. However, the influence of turbulence on the collision process is distinct, as becomes evident from the supplementary movie and figure 1(d), where trajectories of colliding particles are shown. These trajectories originate from a cone-shaped region that is notably larger than the corresponding collision radius r_c , based on the grazing trajectory in quiescent flow. Correspondingly, the collision angle relative to the direction of the imposed bubble velocity is found to be wider in the turbulent flow (see Appendix A). Nevertheless, the collision trajectories appear to follow straight paths towards the bubble, and the colliding particle stream exhibits a band-like pattern, as shown in figure 1(e), both of which are consistent with our modelling assumptions.

For quiescent flow, the dependence of E_c , normalised by the result for tracer particles $E_c(Re_b, 0)$, on Re_b and St_p is presented in figure 2(a). For very small St_p , the inertial effect is negligible and the particles follow the flow streamlines, so that interception is the dominant factor determining the number of collisions in this range (Dai *et al.* 2000).

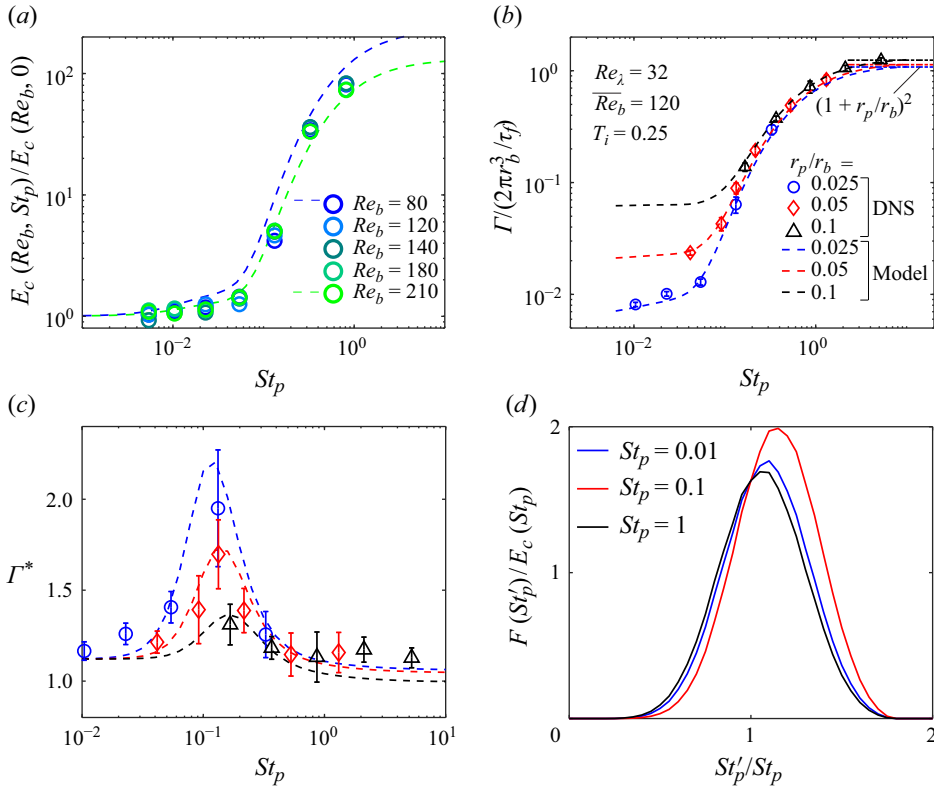


Figure 2. (a) Normalised E_c as a function of St_p in quiescent flow for various Re_b compared to the fits according to (4.1) (dashed lines). (b) Dimensionless collision kernel versus St_p at $\overline{Re}_b = 120$ for bubble with imposed velocity in HIT (symbols) and model (dashed lines). (c) Turbulent collision kernel relative to that in quiescent flow for the imposed velocity bubble. Error bars represent fluctuations between subsets of the data. (d) Scaled PDF of St'_p as a function of St'_p/St_p for different St_p .

Analytical predictions based on flow streamlines in quiescent flow indicate that Γ scales with $(r_p/r_b)^2$ (Weber & Paddock 1983) in this case. However, as particle inertia becomes more pronounced, particles deviate from the flow streamlines and collide on the bubble even if their initial position is outside the grazing trajectory of the inertialess particle. This leads to a higher collision rate and explains the rapid increase in E_c as St_p approaches 0.1, beyond which the inertial effect dominates. At very large St_p , the particles are barely influenced by the flow such that E_c approaches $(1 + r_p/r_b)^2$. To be able to evaluate $E_c(Re_b, St_p)$ analytically, we employ an empirical expression, which is the sum of its two contributions: interceptional collision E_i and the collision associated with particle inertia (Schulze 1989):

$$E_c = E_i + \left(1 + \frac{r_p}{r_b}\right)^2 \left(\frac{St_p}{St_p + a}\right)^b \left(\chi - \frac{E_i}{(1 + r_p/r_b)^2}\right). \quad (4.1)$$

Here, we adopt $E_i = \frac{3}{2}(r_p/r_b)^2(1 + Re_b^{2/3}/5)$ (Sarrot *et al.* 2005) for the collision efficiency in the tracer limit, and the fitting parameters are set to $a = 0.2$ and $b = 2$. Also, $\chi = 1 - 0.9 \times 10^{-((\log(St) + 1.3)/1.6)^2}$ is a fitting correction term to better capture the

transition around $St_p \approx 0.1$. The resulting fit is in good agreement with the data for the evaluated parameter range, as shown in [figure 2\(a\)](#).

As shown for the case with constant bubble velocity in [figure 2\(b\)](#), the general trends of Γ in turbulence, in particular the increase with increasing St_p for all particle sizes, are consistent with those observed in quiescent flow. In this simplified configuration, the PDF of the U'_b required to evaluate our model (2.2) can be obtained by combining the constant bubble rise velocity with the Gaussian distribution of turbulent velocity fluctuations. The collision kernel predicted in this way is in excellent agreement with the simulations. This is further confirmed in [figure 2\(c\)](#), where we scrutinise the result by plotting it relative to the collision kernel at the same bubble velocity in quiescent flow as $\Gamma^* = \Gamma/\Gamma^q$. In this way, it also becomes clear that turbulent flow significantly enhances the collision kernel. Here, two interesting aspects should be underscored. First, Γ^* surpasses 1 when inertia is negligible ($St_p \ll 1$), indicating that turbulent fluctuations enhance interceptional bubble-particle collision. Second, the collision enhancement is not uniform across the considered range of St_p , suggesting that the combined influence of turbulence and particle inertia leads to further amplification of the collision rate. The collision enhancement can reach approximately 100 % for particles with size ratio $r_p/r_b = 0.025$. For larger particles, the maximum collision enhancement is lower, though the peak still occurs at a similar value $St_p \approx 0.1$.

The good agreement with the simulations indicates that the model adequately captures the relevant turbulence effects on the collisions, enabling us to explore their origin. We notice that due to the increase of E_c with increasing Re'_b , the integrand in (2.2) depends nonlinearly on U'_b . This results in an increase in the predicted collision rate even if $f(U'_b)$ is symmetric around \overline{U}_b . In the present case, this effect amounts to almost a 15 % increase in Γ , consistent with what is observed at low St_p .

In addition, there is an inertial effect as a change in U'_b also changes St'_p . The strongly nonlinear dependence of E_c on St'_p , especially in the intermediate range $St_p \approx 0.1$, leads to an asymmetric response to positive and negative velocity fluctuations. This is demonstrated by the scaled PDF of St'_p , $F(St'_p) = E_c(St'_p) \text{PDF}(St'_p)$, shown in [figure 2\(d\)](#). For low and high St_p , the dependence of $F(St'_p)$ on St'_p is almost symmetric. However, for an intermediate value $St_p \approx 0.1$, the contribution to collisions from fluctuating St'_p exhibits a positive bias, which explains the strongly enhanced turbulent collision rate in this range, and the non-monotonic dependence on St_p . Due to the higher interceptional collision efficiency, the increase in the inertial range – and hence the turbulent enhancement – is less pronounced for larger size ratios r_p/r_b .

Another way to validate the model is to consider the spatial distribution of the collision probability $P(r, l)$, where r and l are distances perpendicular to and along the bubble velocity direction, respectively (see [figure 3\(a\)](#)). In quiescent flow, the collision process is deterministic and the collisions probability is a binary function, which has a tube shape based on the grazing trajectory (see the shaded region in [figure 3\(a\)](#)). We represent this using the binary function $S(r, l; U_b)$, which is equal to 1 inside the collision tube, and 0 otherwise, as shown in [figure 3\(a\)](#). Practically, S can be determined from the grazing trajectory. Based on the ‘frozen turbulence’ assumption, the collision probability in turbulence can be predicted as the superposition of the binary probability distributions corresponding to the instantaneous slip velocity U'_b . This leads to

$$P(r, l) = \int f(U'_b) S(r, l; U'_b) G(r, l, U'_b) dU'_b. \quad (4.2)$$

Note that the additional factor $G(r, l, U'_b) = \theta(r, l, U'_b)/2\pi$ in (4.2) is a geometrical coefficient related to the azimuthal integration required for the projection onto the

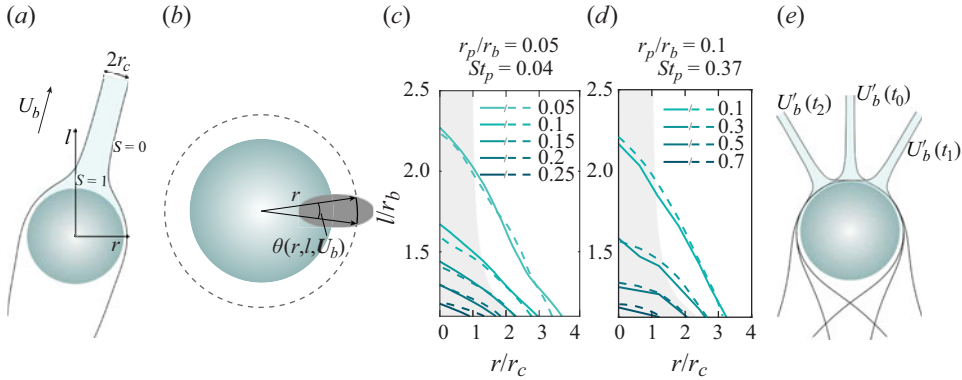


Figure 3. (a) Sketch of the bubble–particle collision with temporary slip velocity U_b' . The blue shaded region indicates the binary function $S(r, l, U_b')$, which is the projection of the collision tube on the $r-l$ plane. (b) Sketch of the cross-section (grey region) between the collision tube and the plane l in the view along the l -axis. Here, $\theta(r, l, U_b')$ indicates the radian of the arc that occupied by the grey region in the circle of radius r , which is used to measure the term $G(r, l, U_b')$. (c,d) Contour lines of $P(r, l)$ from simulations (solid) and model (dashed lines) for $(r_p/r_b = 0.05, St_p = 0.04)$ and $(r_p/r_b = 0.1, St_p = 0.37)$, respectively. (e) Sketch of the collision probability under different bubble slip velocities. The region with more overlaps corresponds to the one with higher collision probability.

two-dimensional (r, l) space. It measures the fraction of the circle with radius r that falls inside the collision tube at distance l , as illustrated in figure 3(b). The result of the model prediction according to (4.2) is again in excellent agreement with the data as shown in figures 3(c) and 3(d), confirming that the basic physical processes are well represented in the model. Consistent with figure 1(d), the impact of turbulence is clearly evident, leading to a much wider distribution of $P(r, l)$ compared to the binary distribution in quiescent flow. This effect is especially pronounced if St_p is low, as is the case for figure 3(c). The collision efficiency is low, and the associated collision stream tube is slender for this case, such that fluctuations in the instantaneous bubble slip direction lead to low values of $P(r, l)$ even close to the bubble surface, as is illustrated in figure 3(e). Since the collision efficiency increases for larger St_p and the collision tube widens, this effect becomes less strong, and the values of the collision probability close to the bubble are much higher in the plot for $St_p = 0.37$ in figure 3(d).

Having established the general suitability of the model to capture the relevant turbulence effects on the collision rate, we now turn to the more realistic case of a freely rising bubble. The corresponding results in terms of Γ are shown in figures 4(a,b) for different Re_λ . In these cases, the bubble slip velocity PDF $f(U_b')$ required as input for the model is measured by averaging the fluid velocity located on a spherical surface of radius $3r_b$ that is centred at the bubble's centre position (Kidanemariam *et al.* 2013). The size of the spherical surface is chosen in a way such that the fluid velocity is not significantly influenced by the presence of the bubble boundary. The radius $3r_b$ of the spherical surface is tested in the case of uniform flow past a fixed sphere (Kidanemariam *et al.* 2013), which results in a measured fluid velocity corresponding to approximately 90 % of the incoming flow velocity.

The general agreement between Γ predicted by the model (dashed lines in figures 4a,b) and the data remains good also for the free rising cases. Difference arises at low St_p , where

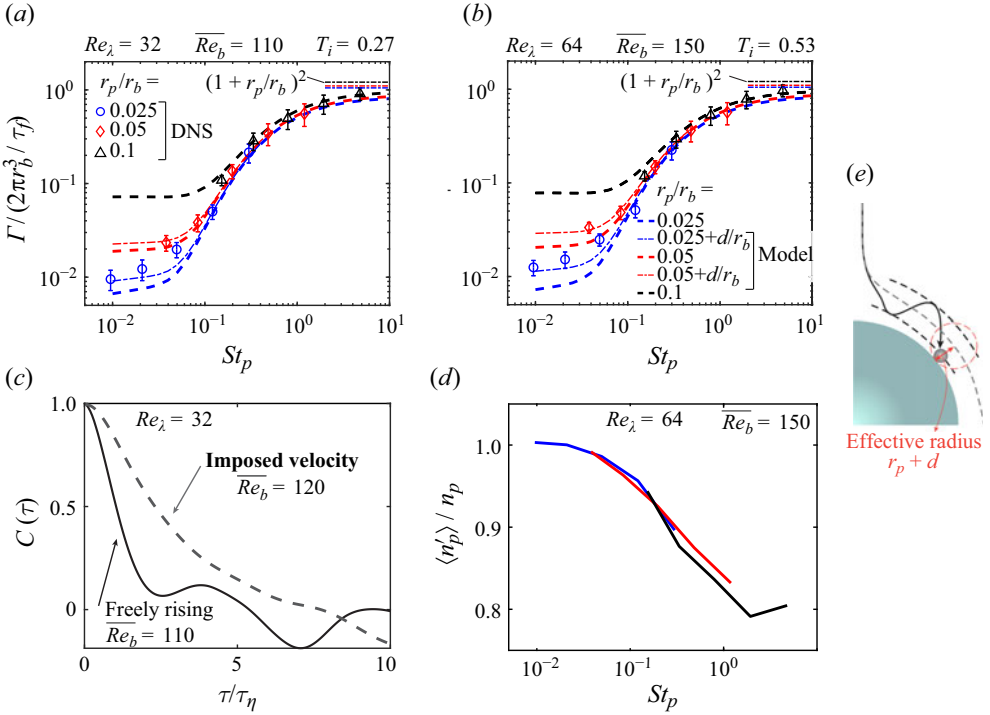


Figure 4. Normalised collision kernel for the freely rising bubble at (a) $Re_\lambda = 32$, $\overline{Re}_b = 110$ and (b) $Re_\lambda = 64$, $\overline{Re}_b = 150$. (c) Comparison of auto-correlation function of U'_b for the imposed velocity ($Re_\lambda = 32$, $\overline{Re}_b = 120$) and freely rising bubbles ($Re_\lambda = 32$, $\overline{Re}_b = 110$), respectively. (d) The normalised mean incoming particle number density as a function of St_p at $Re_\lambda = 64$. (e) Sketch in the bubble reference frame, showing how fluctuations U'_b during the interaction effectively enlarge the particle collision radius.

the model is found to underpredict the simulation result. This can be explained by the correlation time of U'_b , which is shorter for free rising bubbles compared to the imposed velocity case (see figure 4c). The resulting changes in U'_b during the bubble–particle interaction cause the particle trajectory to fluctuate in the bubble frame of reference (see the sketch in figure 4e). This increases the effective collision radius of the particle to $r_p + d$, where d is a measure of the drift from the original particle trajectory. The relevant time and velocity scales for this drift are τ_f and u_η , respectively, such that $d \sim \tau_f u_\eta$ in analogy to Taylor dispersion in the ballistic regime (Taylor 1922). Indeed, we find that using $d = 0.06\tau_f u_\eta$ results in good agreement with our data across different Re_λ and for different r_p , as shown by the dash-dotted lines in figures 4(a,b). This effect is relevant only at $St_p \lesssim 0.1$, and becomes negligible once $r_c \gg d$ due to the inertial effect at larger St_p .

Another finding is that the incoming particle number density can differ from the global value. This is caused by clustering of bubbles and particles in different regions of the flow, leading to segregation (Chan *et al.* 2023). As a result, $\langle n'_p \rangle / n_p$ shown in figure 4(d) decreases as St_p increases, reaching minimum value of approximately 0.8 for $St_p \approx 1$, where clustering effects are known to be strongest. The segregation effect explains why the inertial limit $(1 + r_p/r_b)^2$ at high St_p is not reached in the simulations and in the model, where this effect is accounted for by multiplying with the factor $\langle n'_p \rangle / n_p$ obtained from the simulations.

5. Conclusions

We have elucidated the relevant mechanisms governing the collision rate of inertial particles with a finite-size bubble in turbulence. We demonstrated that for the investigated practical conditions, inertial effects induced by the flow around the bubble are the dominant effect. The nonlinear dependence of these effects on the bubble slip velocity leads to an increase of the collision rate in turbulence of up to 100 % at $St_p \approx 0.1$ compared to quiescent flow. An additional increase in the turbulent collision rate is due to the short temporal correlation of the bubble slip velocity in the free-rising case. The effect of the resulting fluctuations during the bubble–particle interaction can be captured by an increase in the effective collision radius of the particle, and is mostly relevant in the tracer limit for $St_p \lesssim 0.1$. Segregation of bubbles and particles in turbulence reduces the particle density encountered by the bubble and hence the collision rate by up to 20 % at $St_p \approx 1$. Remarkably, the effect of turbulence-induced motion of the particles was found to have negligible impact during the transient bubble–particle interaction, whereas the incoming particle number density is reduced for particles with large Stokes number. The developed frozen turbulence model provides a physically consistent framework that can be easily extended to a full collision model (by combining it with a prediction for $f(U'_b)$). The approach is also transferable to other conditions, such as more complex shapes (by adopting a different parametrisation of E_c), and thus offers a more general relevance for collisions with finite-size objects in turbulence.

Supplementary movie. Supplementary movie is available at <https://doi.org/10.1017/jfm.2025.44>.

Acknowledgements. We thank Timothy Chan and Duco van Buuren for fruitful discussions. This project has received funding from the European Research Council (ERC) under the European Union's Horizon 2020 research and innovation programme (grant agreement no. 950111, BU-PACT). This work was carried out on the Dutch national e-infrastructure with the support of SURF Cooperative.

Declaration of interests. The authors report no conflict of interest.

Appendix A

As we observe that the trajectories of collided particles in HIT are significantly different from those in quiescent flow, it is interesting to study how turbulence affects the collision angle. In [figure 5](#), we investigate the collision angle θ for the case where the bubble velocity is imposed. Here, θ denotes the angle between the direction of the imposed bubble velocity and the vector of collision position in the bubble frame. We observe that the mean collision angle $\langle\theta\rangle$ for the turbulence flow is higher than that for the case of quiescent flow. However, $\langle\theta\rangle$ shows a similar dependence on St_p for both cases, where $\langle\theta\rangle$ first decreases as St_p , and rises after. This can be explained by inertial effects on the particles as illustrated in [figures 5\(b\)](#) and [5\(c\)](#) for the deterministic case. At low St_p , r_c is small. Consequently, particles collide on the bubble front region, where the streamlines are strongly curved. Therefore, particle trajectories deviate significantly from the streamlines as St_p increases. As a consequence, higher-inertia particles collide at a smaller collision angle, as illustrated in [figure 5\(b\)](#). When St_p surpasses the critical value, r_c becomes larger. In this case, increasing particle inertia leads to a higher collision rate as well as to a higher collision angle, which is illustrated in [figure 5\(c\)](#). These general trends for $\langle\theta\rangle$ are retained in the turbulent case, which is in line with our approach of representing the instantaneous collision process by the deterministic case. [Figures 5\(d–f\)](#) show the scaled PDF of collision angle θ for different particle sizes. The scaled PDF illustrates the distribution of the collision angle, as well as where the collision differences occur between

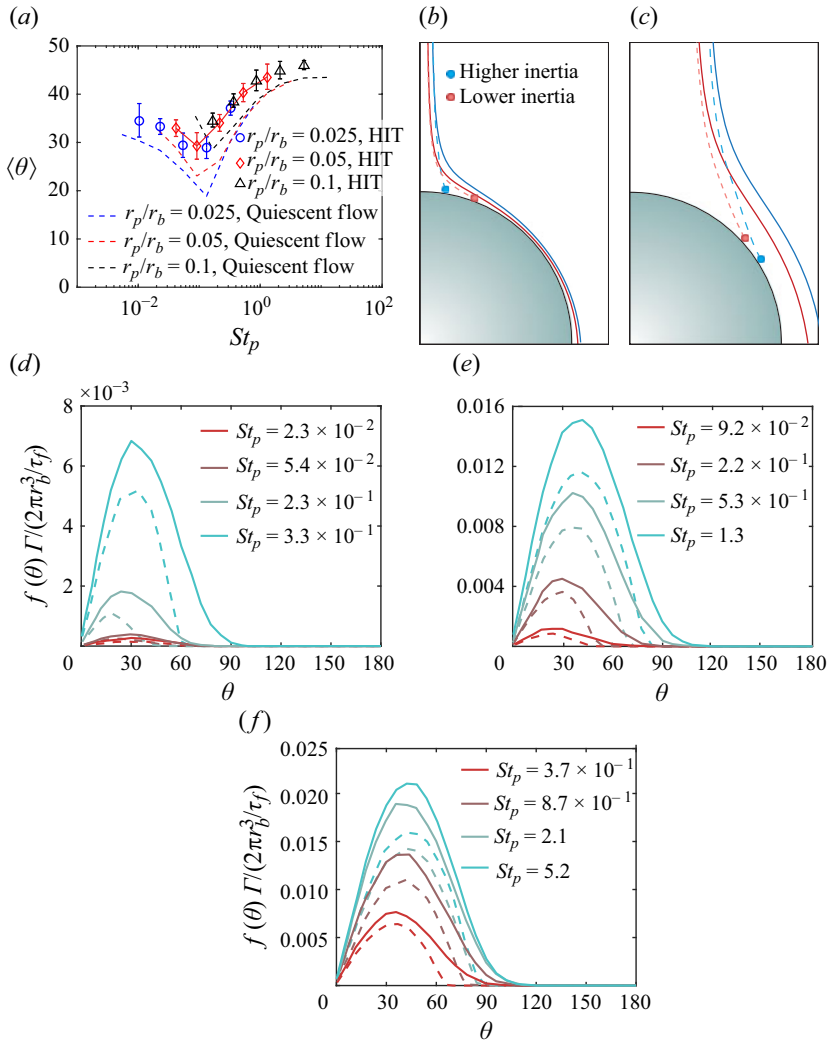


Figure 5. (a) Mean collision angle $\langle\theta\rangle$ as a function of St_p . (b,c) Sketches illustrate the mechanism that $\langle\theta\rangle$ declines/increases as increasing inertia when St_p is low/high in quiescent flow. The solid lines denote the streamlines along which the particles originally stay, and the dashed lines are the particle trajectories. (d–f) The PDFs of collision angle $f(\theta)$ scaled by the normalised collision kernel for particle size $r_p/r_b = 0.025, 0.05, 0.1$ in HIT (solid lines) and quiescent flow (dashed lines).

HIT and quiescent flow. The distributions of collision angle indicate that the collisions are more likely to take place at intermediate angles. Moreover, we observe that the distribution extends to a wider range in HIT, and more collisions occur, which is consistent with the observations for $\langle\theta\rangle$.

REFERENCES

- ABRAHAMSON, J. 1975 Collision rates of small particles in a vigorously turbulent fluid. *Chem. Engng Sci.* **30** (11), 1371–1379.
- ARGUEDAS-LEIVA, J., SŁOMKA, J., LALESCU, C.C., STOCKER, R. & WILCZEK, M. 2022 Elongation enhances encounter rates between phytoplankton in turbulence. *Proc. Natl. Acad. Sci.* **119** (32), e2203191119.

- BLOOM, F. & HEINDEL, T.J. 2002 On the structure of collision and detachment frequencies in flotation models. *Chem. Eng. Sci.* **57** (13), 2467–2473.
- CALZAVARINI, E. 2019 Eulerian–Lagrangian fluid dynamics platform: the ch4-project. *Softw. Impacts* **1**, 100002.
- CHAN, T., NG, C.S. & KRUG, D. 2023 Bubble–particle collisions in turbulence: insights from point-particle simulations. *J. Fluid Mech.* **959**, A6.
- CHOUPPE, A. & UHLMANN, M. 2015 Forcing homogeneous turbulence in direct numerical simulation of particulate flow with interface resolution and gravity. *Phys. Fluids* **27** (12), 123301.
- CUSHING, R.S. & LAWLER, D.F. 1998 Depth filtration: fundamental investigation through three-dimensional trajectory analysis. *Environ. Sci. Technol.* **32** (23), 3793–3801.
- DAI, Z., FORNASIERO, D. & RALSTON, J. 2000 Particle–bubble collision models – a review. *Adv. Colloid Interface Sci.* **85** (2–3), 231–256.
- DERJAGUIN, B.V. & DUKHIN, S.S. 1993 Theory of flotation of small and medium-size particles. *Prog. Surf. Sci.* **43** (1), 241–266.
- FALKOVICH, G., FOUXON, A. & STEPANOV, M.G. 2002 Acceleration of rain initiation by cloud turbulence. *Nature* **419** (6903), 151–154.
- GUILLOT, T., IDA, S. & ORMEL, C.W. 2014 On the filtering and processing of dust by planetesimals– I. Derivation of collision probabilities for non-drifting planetesimals. *Astron. Astrophys.* **572**, A72.
- HAJISHARIFI, A., MARCHIOLI, C. & SOLDATI, A. 2021 Particle capture by drops in turbulent flow. *Phys. Rev. Fluids* **6** (2), 024303.
- HÖFLER, K. & SCHWARZER, S. 2000 Navier–Stokes simulation with constraint forces: finite-difference method for particle-laden flows and complex geometries. *Phys. Rev. E* **61** (6), 7146–7160.
- HOMANN, H., GUILLOT, T., BEC, J., ORMEL, C.W., IDA, S. & TANGA, P. 2016 Effect of turbulence on collisions of dust particles with planetesimals in protoplanetary disks. *Astron. Astrophys.* **589**, A129.
- HUANG, Z., LEGENDRE, D. & GUIRAUD, P. 2012 Effect of interface contamination on particle–bubble collision. *Chem. Eng. Sci.* **68** (1), 1–18.
- JIANG, L., WANG, C., LIU, S., SUN, C. & CALZAVARINI, E. 2022 Dynamics of finite-size spheroids in turbulent flow: the roles of flow structures and particle boundary layers. *J. Fluid Mech.* **939**, A22.
- JOHNSON, T.A. & PATEL, V.C. 1999 Flow past a sphere up to a Reynolds number of 300. *J. Fluid Mech.* **378**, 19–70.
- KIDANEMARIAM, A.G., CLEMENS, C.B., DOYCHEV, T. & UHLMANN, M. 2013 Direct numerical simulation of horizontal open channel flow with finite-size, heavy particles at low solid volume fraction. *New J. Phys.* **15** (2), 025031.
- KOH, P.T.L. & SCHWARZ, M.P. 2007 CFD model of a self-aerating flotation cell. *Intl J. Miner. Process.* **85** (1), 16–24.
- KOSTOGLU, M., KARAPANTSIOS, T.D. & EVGENIDIS, S. 2020a On a generalized framework for turbulent collision frequency models in flotation: the road from past inconsistencies to a concise algebraic expression for fine particles. *Adv. Colloid Interface Sci.* **284**, 102270.
- KOSTOGLU, M., KARAPANTSIOS, T.D. & OIKONOMIDOU, O. 2020b A critical review on turbulent collision frequency/efficiency models in flotation: unravelling the path from general coagulation to flotation. *Adv. Colloid Interface Sci.* **279**, 102158.
- LIU, T.Y. & SCHWARZ, M.P. 2009 CFD-based multiscale modelling of bubble–particle collision efficiency in a turbulent flotation cell. *Chem. Eng. Sci.* **64** (24), 5287–5301.
- MAY, K.R. & CLIFFORD, R. 1967 The impactation of aerosol particles on cylinders, spheres, ribbons and discs. *Ann. Occup. Hyg.* **10** (2), 83–95.
- MITTAL, R. & IACCARINO, G. 2005 Immersed boundary methods. *Annu. Rev. Fluid Mech.* **37** (1), 239–261.
- NGUYEN, A. & SCHULZE, H.J. 2003 *Colloidal Science of Flotation*. CRC Press.
- NGUYEN, A.V., AN-VO, D.A., TRAN-CONG, T. & EVANS, G.M. 2016 A review of stochastic description of the turbulence effect on bubble–particle interactions in flotation. *Intl J. Miner. Process.* **156**, 75–86.
- PERLEKAR, P., BIFERALE, L., SBRAGAGLIA, M., SRIVASTAVA, S. & TOSCHI, F. 2012 Droplet size distribution in homogeneous isotropic turbulence. *Phys. Fluids* **24** (6), 065101.
- PESKIN, C.S. 2002 The immersed boundary method. *Acta Numerica* **11**, 479–517.
- POYDENOT, F. & ANDREOTTI, B. 2024 Gap in drop collision rate between diffusive and inertial regimes explains the stability of fogs and non-precipitating clouds. *J. Fluid Mech.* **987**, A37.
- PUMIR, A. & WILKINSON, M. 2016 Collisional aggregation due to turbulence. *Annu. Rev. Condens. Matter. Phys.* **7** (1), 141–170.
- PYKE, B., FORNASIERO, D. & RALSTON, J. 2003 Bubble particle heterocoagulation under turbulent conditions. *J. Colloid Interface Sci.* **265** (1), 141–151.

- SAFFMAN, P.G. & TURNER, J.S. 1956 On the collision of drops in turbulent clouds. *J. Fluid Mech.* **1** (1), 16–30.
- SARROT, V., GUIRAUD, P. & LEGENDRE, D. 2005 Determination of the collision frequency between bubbles and particles in flotation. *Chem. Eng. Sci.* **60** (22), 6107–6117.
- SCHULZE, H.J. 1989 Hydrodynamics of bubble–mineral particle collisions. *Miner. Process. Extr. Metall. Rev.* **5** (1), 43–76.
- TAYLOR, G.I. 1922 Diffusion by continuous movements. *Proc. Lond. Math. Soc.* **2** (1), 196–212.
- TSCHISGALE, S., KEMPE, T. & FRÖHLICH, J. 2017 A non-iterative immersed boundary method for spherical particles of arbitrary density ratio. *J. Comput. Phys.* **339**, 432–452.
- UHLMANN, M. 2005 An immersed boundary method with direct forcing for the simulation of particulate flows. *J. Comput. Phys.* **209** (2), 448–476.
- WANG, A., HOQUE, M.M., EVANS, G. & MITRA, S. 2022 Effect of turbulence dispersion on bubble–particle collision efficiency. *Miner. Engng* **177**, 107374.
- WEBER, M.E. & PADDOCK, D. 1983 Interceptional and gravitational collision efficiencies for single collectors at intermediate Reynolds numbers. *J. Colloid Interface Sci.* **94** (2), 328–335.
- YOON, R.H., SONI, G., HUANG, K., PARK, S. & PAN, L. 2016 Development of a turbulent flotation model from first principles and its validation. *Intl J. Miner. Process.* **156**, 43–51.